# Dark current suppression in HOT LWIR HgCdTe heterostructures operating in non-equilibrium mode

Martyniuk P[1*], Gawron W[1], Pawluczyk J[2], Kębłowski A[2], Madejczyk P[1], Rogalski A[1]

(1. Institute of Applied Physics, Military University of Technology, 2 Kaliskiego Str. , 00-908 Warsaw, Poland;

2. Vigo System S. A. , 129/133 Poznańska Str. , 05-850 O żarów Mazowiecki, Poland)

**Abstract**：Typically, infrared detectors require cryogenic cooling to limit dark current which is directly dependent on Auger generation-recombination mechanism and highly influential in HgCdTe-narrow band gap material. The Auger suppressed architectures have an advantage over conventional detectors allowing operation at elevated temperatures > 200 K. Architecture with combination of exclusion and extraction heterojunctions has been proposed to lower Auger contribution. The paper presents a new long-wave ( ≈ 10 μm) infrared HgCdTe architecture with graded gap/doping interfaces and extra barrier located in exclusion heterojunction to suppress dark current for high operating temperature conditions. Proper barrier implementation reduces dark current by more than 20 A/cm$^2$ for room temperature operation.

**Key words**：HOT, HgCdTe, non-equilibrium conditions, barrier infrared detectors

**PACS**：85. 60. Gz

## Introduction

Higher operation temperature (HOT) condition of the long (8-12 μm) wavelength (LWIR) photodetectors without lowering the performance is considered to be an universal goal and one of the most important research area in infrared technology driven by applications requiring high detectivity and fast response operation[1]. The weight, cost and reliability problems associated with the cooling mechanisms restricts the application potential of these devices. At elevated temperatures ( > 200 K), reached by thermoelectric coolers, dark current is mostly limited by Auger generation-recombination (GR) mechanism, where low doped active layers turn to be intrinsic especially in narrow bandgap materials leading to increase of the carrier concentration above doping level. In practice, to circumvent this problem, most of HgCdTe photodiodes are based on $N^+ p(\pi) P^+$ reversely biased heterostructures allowing to reduce carrier concentrations below thermal equilibrium and to prevent parasitic thermal generation at contacts, surfaces and interfaces[2-8]. These special heterostructure designs are developed and extended with interface layers, where $p(\pi)$-type absorber is advantageous in comparison with structure $N^+ n(v) P^+$ due to both high diffusion and drift ambipolar mobility. Additionally, $p(\pi)$-type HgCdTe active regions are characterized by the best compromise between requirement of the high quantum efficiency and a low thermal generation driven by the Auger 7 GR mechanism, where non-equilibrium conditions could be easily implemented[9,10]. In our laboratory, $N^+ p(\pi) P^+$ complex multi-layer structures with properly designed interfaces has been used with great success for LWIR range photodiodes operating under non-equilibrium mode at HOT conditions[11-14]. In this paper we present the new LWIR ( ≈ 10 μm) detector architecture with extra barrier located in $P^+$ ($\pi$-$P^+$ exclusion heterojunction) region to suppress dark current. Detector structure was simulated with software APSYS by Crosslight Inc. The voltage and structural dependences of the dark current charac-

teristics, including both trap-assisted (TAT) and band to band (BTB) tunnelling processes at the heterojunctions were modelled and compared to experimental results showing potential capability of extra barrier incorporation, suppressing dark current more than 20 A/cm$^2$ at room temperature operation depending on the $P^+$ region composition.

## 1  Simulation procedure

The simulated 11 layer $N^+/P1/\pi/P2/B/P^+/p^+/n^+$ (sample 2) structure with extra barrier (B) in $p(\pi)$-$P^+$ heterojunction, absorber composition of $x = 0. 175$, its thickness of $t ≈ 4. 9$ μm, and p-type doping ($N_A = 7 \times 10^{15}$ cm$^{-3}$) is shown in Fig. 1. Structural parameters such as constituent layers' thickness, doping and composition were marked by black arrows. The $p^+/n^+$ ($N_A = N_D = 2 \times 10^{17}$ cm$^{-3}$, $x = 0. 3 \sim 0. 15$) junction has been applied for improvement of electrical contact property between $P^+$ region and metallization. $N^+$-$n^+$ contact doping and composition was assumed in the range 0. 39-0. 22, $N_D = 2 \times 10^{17}$-$2 \times 10^{16}$ cm$^{-3}$, respectively. Interface 1 (P1) and 2 (P2) p-type layers were graded to fit to the absorber layer $x = 0. 22 \sim 0. 175$ and 0. 175 $\sim$ 0. 3, respectively. Mentioned structure with extra barrier was compared with conventional architecture $N^+/P1/\pi/P2/P^+/p^+/n^+$ (sample 1) assuming the same structural parameters in terms of dark current reduction. The devices presented in this paper were fabricated and characterized in joint laboratory run by VIGO System S. A. and Military University of Technology (MUT). The (111) HgCdTe epiready layers were grown on 2" inch semi-insulating, slightly disoriented (100) GaAs substrates in a horizontal MOCVD AIX 200 reactor. The interdiffused multilayer process (IMP) technique was applied for the HgCdTe layer's deposition. The detailed description of the MOCVD growth procedure may be found in Refs. 15 and 16.

The secondary ion mass spectroscopy (SIMS) measurements presented in Fig. 2 performed with Cs$^-$ (a) and Cs$^+$ (b) ions were
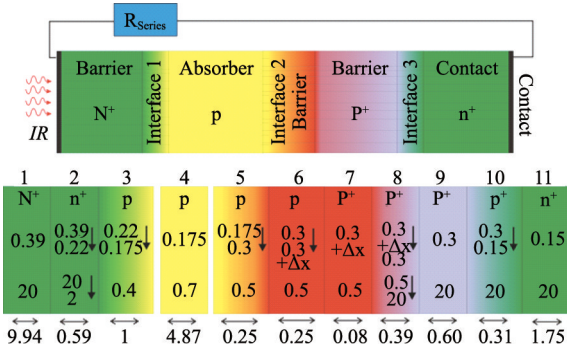
Fig. 1 Simulated graded gap HgCdTe heterostructure with extra barrier in P$^+$ region. The layer number, type of doping, composition grading, doping grading $\times 10^{16}$ cm$^{-3}$, and thickness of the layers in μm are marked. Sample 2



Fig. 2 SIMS profile of the HgCdTe heterostructure: Cs$^-$(a) and Cs$^+$(b) for sample 2

used to verify the compositional and doping profiles of the simulated structure (sample 2). Depending on the Cs ions, two slightly different P$^+$ region and active layer compositions were estimated. Assuming Cs$^-$, P$^+$ region composition was found to be $x \approx 0.3$, while for Cs$^+$ more than 0.4, respectively. In both cases extra barrier composition in P$^+$ region was in the range of $\Delta x = 0.05$ ($x = x_{P+} + 0.05$).

Nominal pre-growth extra barrier composition and doping was assumed to be $\Delta x = 0.39$, $N_A = 2 \times 10^{15}$ cm$^{-3}$ and thickness, $t = 0.08$. SIMS measurements for As concentration in extra barrier region suggests $N_A$ doping in range of $\sim 10^{16}$-$2 \times 10^{17}$ cm$^{-3}$. The calculations were carried out for lower extra barrier doping, $N_A = 5 \times 10^{15}$ cm$^{-3}$, because doping level $< 10^{16}$ cm$^{-3}$ allows to observe required $J_{DARK}$ dependence on voltage and selected compositions $\Delta x = 0$-$0.35$ (for P$^+$, $x = 0.3$). In simulations we also used lower composition of absorber layer, $x = 0.175$. The measured spectral response characteristics at equilibrium and for $V = -400$ mV (N$^+$/P1/π/P2/P$^+$/p$^+$/n$^+$) and $V = -700$ mV (N$^+$/P1/π/P2/B/P$^+$/p$^+$/n$^+$) give $\lambda_{Peak} \approx 7.2$ μm and responsivity within the range of $0.1 \sim 0.2$ and $8 \sim 12$ A/W, respectively. The cut-off wavelength assumes $\lambda_c \approx 10$ μm at $T = 300$ K suggesting that active region composition was assumed in proper range $x = 0.175$ in both samples 1 and 2, respectively.
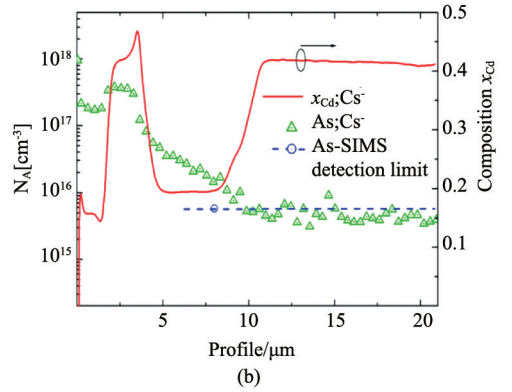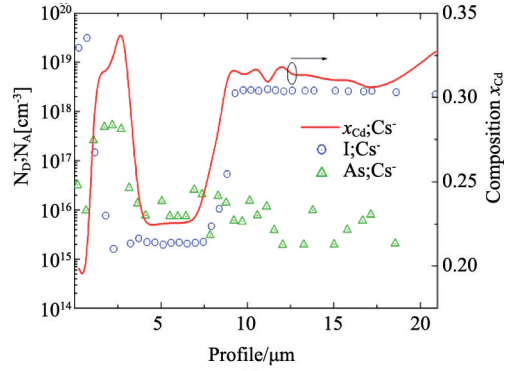
Theoretical modeling of the HgCdTe heterostructures was performed by numerical solving of the Poisson's equation and the electron/hole current continuity equations by APSYS platform (Crosslight Inc.). APSYS uses the Newton-Richardson method of nonlinear iterations[17]. The applied model incorporates both HgCdTe electrical and optical properties by taking into account influence of radiative (RAD), Auger (AUG), Shockley-Read-Hall (SRH) GR and BTB as well as TAT tunnelling mechanisms at any location within the device. After Casselman et al., we incorporated AUG GR mechanisms using parabolic bands and non-degenerate statistics, which are considered to be suitable approximations for modelled device[18]. In TAT simulation, the Hurkx et al. model was implemented[19]. APSYS platform requires the input of

**Table 1 Parameters taken in modeling of LWIR N$^+$/P1/π/P2/P$^+$/p$^+$/n$^+$ and N$^+$/P1/π/P2/B/P$^+$/p$^+$/n$^+$ type detectors**

| | 1/2 | 3 | 4 | 5 | 6 | 7 | 8 | 9 | 10/11 |
|---|---|---|---|---|---|---|---|---|---|
| | N$^+$/n$^+$ | p | p | p | p | P | P$^+$ | P$^+$ | P$^+$/n$^+$ |
| $N_A, N_D$/cm$^{-3}$ | $2 \times 10^{17} \rightarrow 2 \times 10^{16}$ | $2 \times 10^{16} \rightarrow 4 \times 10^{15}$ | $7 \times 10^{15}$ | $5 \times 10^{15}$ | $5 \times 10^{15}$ | $5 \times 10^{15}$ | $5 \times 10^{15} \rightarrow 2 \times 10^{17}$ | $2 \times 10^{17}$ | $2 \times 10^{17}$ |
| Gauss tail, d$x$/μm | 0.05 | 0.05 | 0.05 | 0.05 | 0.05 | 0.02 | 0.02 | 0.02 | 0.02 |
| Composition, $x$ | $0.39 \rightarrow 0.22$ | $0.22 \rightarrow 0.175$ | 0.175 | $0.175 \rightarrow 0.3$-$0.45$ | $0.3$-$0.45 \rightarrow 0.3$-$0.45 + \Delta x$ | $0.3$-$0.45 + \Delta x$ | $0.3$-$0.45 + \Delta x \rightarrow 0.3$-$0.45$ | $0.3$-$0.45$ | $0.3$-$0.45 \rightarrow 0.15$ |
| Geometry, $t$/μm | 10.53 | 1 | 4.87 | 0.25 | 0.25 | 0.08 | 0.39 | 0.6 | 2.06 |
| Area, $A$/μm$^2$ | | | | | $100 \times 100$ | | | | |
| Overlap matrix, $F_1 F_2$ | | | | | 0.27 | | | | |
| Trap energy level, $E_{Trap}$ | | | | | $0.33 \times E_g$ | | | | |
| Trap concentration, $N_{Trap}$/cm$^{-3}$ | | | | | $10^{12}$ | | | | |
| Capture cross section SRH $\frac{\sigma_n}{\sigma_p}$/cm$^2$ | | | | | $\frac{10^{-15}}{10^{-15}}$ | | | | |

HgCdTe material parameters (bandgap, electron affinity, dielectric constant, electron and hole mobility, electron and hole effective mass, and absorption coefficient), which were taken from published models. In particular, the bandgap was obtained from Hansen *et al.* [20]. The low-field electron mobility was taken from the empirical formula based on Scott's paper, while hole mobility was basically taken as 1 % of the electron mobility [21]. In the case of ohmic contacts, simple Dirichlet boundary conditions are applied. The electron and hole quasi-Fermi levels are equal and set to the applied bias of that electrode, i. e. , $E_{fn} = E_{fp} = V$.

HgCdTe is a narrow-gap semiconductor (NGS) exhibiting a non-parabolic conduction band and high carrier degeneracy. These characteristics are very difficult to simulate due to numerical problems associated with the computation of the Fermi-Dirac integral (FDI) [22-23]. Quan *et al.* and Wang *et al.* have proposed simple approximations to FDI being validated for $T = 77 \sim 120$ K [24-26]. The HgCdTe devices simulated in this paper operates at $T = 300$ K and simulations were performed using the Fermi-Dirac statistics for a non-degenerate semiconductor model with parabolic energy bands.

Table 1 shows parameters taken in modeling of LWIR $N^+/P1/\pi/B/P2/P^+/p^+/n^+$ type detectors. P1, P2 and B interface and extra barrier layers were assumed to be $x$-graded regions and represent the real structure which profile is shaped by interdiffusion processes during HgCdTe growth. The doping's profiles were also simulated by applying gauss tail model (see Table 1, Ref. 17). The trap density, $N_{Trap}$, and trap energy level, $E_{Trap}$, were assumed at $N_{Trap} = 5 \times 10^{14}$ cm$^{-3}$ and $E_{Trap} = 0.33 \times E_g$, respectively (counted from conduction band) [27]. The detector's area was estimated as $A = 100$ μm × 100 μm.

## 2   Results and discussion

The modelled energy band diagram profiles of both the LWIR $N^+/P1/\pi/P2/P^+/p^+/n^+$ (a) and $N^+/P1/\pi/P2/B/P^+/p^+/n^+$ with extra barrier $\Delta x = 0.35$ (b) detector's structures are presented in Fig. 3. The $P^+$ region composition was assumed to be $x = 0.3$. The calculations were performed using the reverse bias polarization $V = -1\ 000$ mV. The extra barrier height was estimated in range of ~385 meV at assumed biasing condition. Under reverse voltage polarization, in modelled structure operating in non-equilibrium condition, the electrons are extracted from the absorber region by positive electrode connected to $N^+$-contact layer ($N^+$-$\pi$ heterojunction). The electrons are also excluded from the absorber near the $\pi$-$P^+$ junction because they cannot be injected from negative electrode into $P^+$-layer. The energy barrier between $n^+$ and $P^+$ regions enhance exclusion of electrons from the absorber region and, as a consequence, they cannot be replenished due to the low concentration of the electrons in $P^+$-barrier region.

Extraction $N^+$-$\pi$ heterojunction with $x$-graded sublayers, were found to play dominant role in performance modeling of the mentioned structures. Figure 4 presents electric field ($F$) drop along the sample for three select-
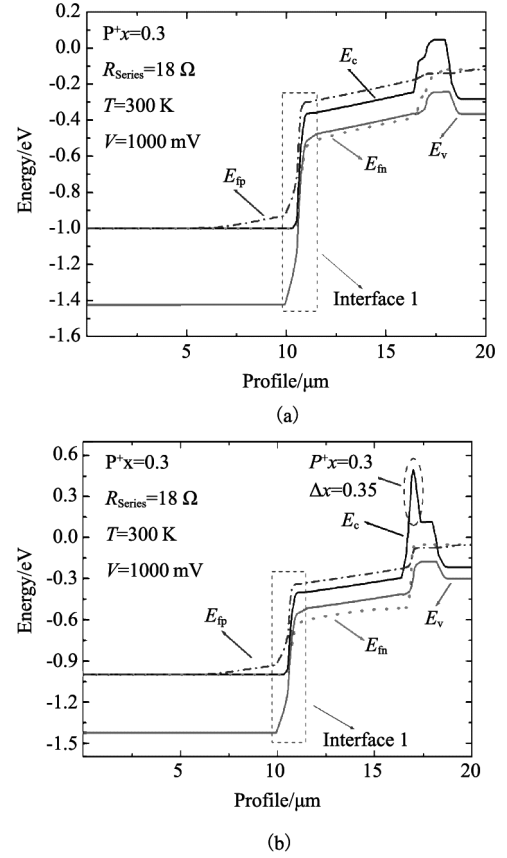


(a)



(b)

Fig. 3   Energy band diagram of LWIR HgCdTe hetrostructure:(a) with $P^+$, $x = 0.3$;(b) with extra barrier $\Delta x = 0.35$ at reverse bias $V = -1\ 000$ mV. $E_{fn}$ and $E_{fp}$ stand for electron and hole quasi-Fermi levels

ed extra barrier compositions $\Delta x$ (0; 0.1 and 0.3) for bias where $J_{DARK}$ versus voltage reaches its minimum ($V_{Min}$) and $P^+$ layer composition, $x = 0.3$. $V_{Min}$ dependence on $\Delta x$ for selected $P^+$ composition is shown in Fig. 4 (c). The higher $\Delta x$ the higher $F$ drops at the $\pi$-$P^+$ exclusion heterojunction, which leads to $F$ decrease at the extraction $N^+$-$\pi$ heterojunction for $\Delta x$ from 0 to 0.1. We also presented profile of the electron concentration ($n$) along the modelled structure calculated for $V_{Min}$. Intrinsic concentration ($n_i$) for simulated active layer was estimated at the level of $4.7 \times 10^{16}$ cm$^{-3}$ ($T = 300$ K). Once we increase $\Delta x$ within the range of 0-0.2 (for $P^+$, $x = 0.3$) non-equilibrium conditions are more visible and electron concentration in the middle of absorber layer ($d = 14$ μm) decreases sharply from $10^{14}$ to $2 \times 10^{13}$ cm$^{-3}$. Above $\Delta x > 0.2$ electron concentration tends to saturate.

The measured and simulated $J_{DARK}$ characteristics are presented in Fig. 5 for $P^+$ layer composition, $x = 0.3$ (a) and $x = 0.4$ (b), respectively. The experimental results were presented for two sets of the detectors (a) and (b) fabricated from the same wafer. Both samples 1 (a,b) and 2 (a,b) exhibit difference in $J_{DARK}$ versus voltage for the region, where TAT and BTB mechanisms contribute to the net current which we attributed to the
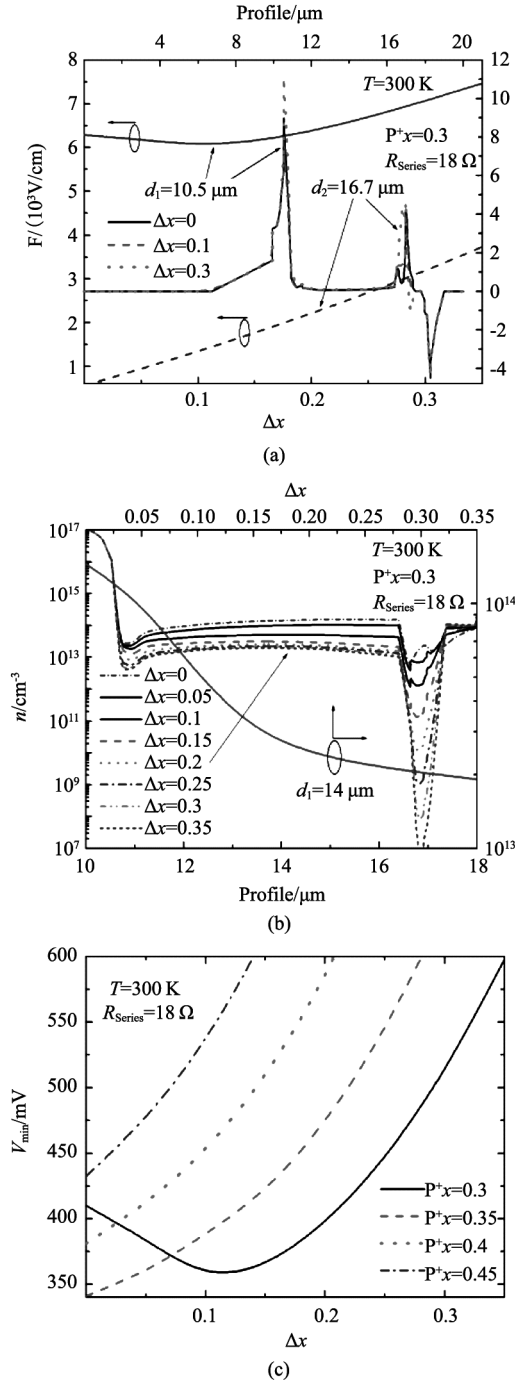
Fig. 4 Electric field drop along the structure and versus extra barrier composition $\Delta x$ (a); electron concentration along the structure and versus extra barrier composition (b); $V_{Min}$ dependence on extra barrier $\Delta x$ (c) for LWIR HgCdTe heterostructure at $T = 300$ K and $R_{Series} = 18$ Ω. $d_1$ and $d_2$ stand for distance along the samples

different $N_{Trap}$ concentrations (*processing* of the samples) according to the Hurks *et al.* model. The series resistance influences the slope of the $J_{DARK}$ characteristics and was found to be at the level of 18 Ω in order to fit to the

experimental results for P$^+$, $x = 0.3$ and barrier $\Delta x = 0.35$, respectively. Analyzing $J_{DARK}$ characteristic for $\Delta x = 0.35$ we reached proper fitting to the experimental results (sample 2), while for the structure with no barrier ($\Delta x = 0$) the simulated maximum of $J_{DARK}$ was found to be ~ 20 A/cm$^2$ higher than measured one, which could be attributed to the assumed lower absorber composition in that device (for the same $R_{Series} = 18$ Ω). It must be noted that fitting to the experimental results could be reached also by assuming different $R_{Series}$ for both detectors, which should be considered as closer to real conditions due to the detector's *processing* and growth procedure. Assuming $\Delta x = 0.05$, the $J_{DARK}$ measured characteristics for sample 2 could be nearly reached with $R_{Series} = 38$ Ω in comparison with sample 1 simulated for $R_{Series} = 18$ Ω.

Both samples exhibit rapid increase of $J_{DARK}$ to $V_{Max} = -353$ and -628 mV, respectively. In this voltage region, differential resistance increases and at final stage becomes infinite. Once $J_{DARK}$ reaches the maximum, $J_{DARK}$ characteristic exhibits negative differential resistance (NDR) as a result of AUG GR suppression. The SRH GR and tunneling mechanism contribute to the net dark current for voltage $V = V_{Min}$. Further increase of the reverse voltage leads to increase of the $J_{DARK}$ due to tunneling effects (TAT) at the decisive N$^+$-π extraction heterojunction. Extra barrier implementation in π-P$^+$ exclusion heterojunction for P$^+$, $x = 0.3$ reduces $J_{DARK}$ more than 20 A/cm$^2$ as far as $V_{Min}$ voltage is concerned. Extraction coefficient increases from 3.8 to 6 for $\Delta x$ within the range of 0 to 0.35. On the other hand, for P$^+$, $x = 0.4$ and 0.45 this effect was not observed. In this case, gradual increase of $J_{DARK}$ is visible. Extra barrier in P$^+$, $x = 0.3$ region allows to reach $J_{Min}$ for lower voltages in comparison with structure with P$^+$, $x = 0.4$. Potentially this would attribute to the fast operation of the structure. Electric field drop along extraction heterojunction is believed to be responsible for this behaviour.

The very last figure presents $J_{Min}$ and $J_{Max}$-$J_{Min}$ versus $\Delta x$ for selected P$^+$ layer composition. For P$^+$, $x = 0.3$, $J_{Min}$ reaches its minimum for extra barrier composition, $\Delta x = 0.175$, while $J_{Max}$-$J_{Min}$ for $\Delta x = 0.16$. The minimum of the $J_{Min}$ is also observed for $\Delta x = 0.1$ (P$^+$, $x = 0.35$), while for $x = 0.4$ and 0.45 this behaviour was not noticed. In the latter case, the simulation results suggest not to use any extra barriers in π-P$^+$ region. In analyzed structure the lowest $J_{Min} \approx 11$ A/cm$^2$ was estimated for P$^+$, $x = 0.4$ with no extra barrier, while for P$^+$, $x = 0.45$ further decrease of the $J_{Min}$ was not observed.

## 3 Conclusion

We simulated and compared two architectures operating in non-equilibrium mode. Extra barrier (in π-P$^+$ exclusion heterojunction) influence on dark current was presented, More than 20 A/cm$^2$ reduction in $J_{DARK}$ can be reached for lower applied voltages. The effect of $J_{DARK}$ suppression with extra barrier contribution was only visible for P$^+$ $x \leqslant 0.35$, while for $x > 0.4$ extra barrier has
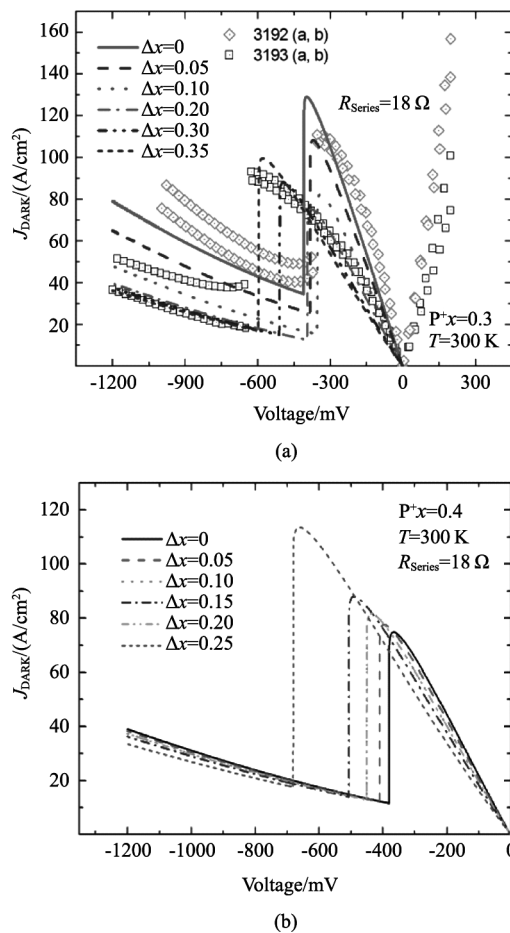
Fig. 5    Measured and simulated $J_{DARK}$ versus voltage
for P$^+$, $x = 0.3$ (a) and P$^+$, $x = 0.4$ (b) for LWIR
HgCdTe heterostructure at $T = 300$ K and $R_{Series} = 18$ Ω

no contribution to $J_{DARK}$ for analyzed structure.

## Acknowledgments

## References

[1] Rogalski A, *Infrared detectors* [M]. CRC Press, Boca Raton,
2011.

[2] Ashley T, Elliott C T. Non-equilibrium mode of operation for
infrared detection [J]. *Electron. Lett.*, 1985, **21**：451-452.

[3] Jaksic Z, Djuric Z. Extraction photodiodes with Auger sup-
pression for all-weather free-space optical communication [J].
*Electronics*, 2004, **8**：30-32.

[4] Emelie P Y, Philips J D, Velicu S, *et al*. Modeling and de-
sign considerations of HgCdTe infrared photodiodes under non-
equilibrium operation [J]. *J. Electron. Mater.*, 2007, **36**：
846-851.

[5] Emelie P Y, Velicu S, Grein C H, *et al*. Modeling of LWIR
HgCdTe Auger-suppressed infrared photodiodes under non-e-
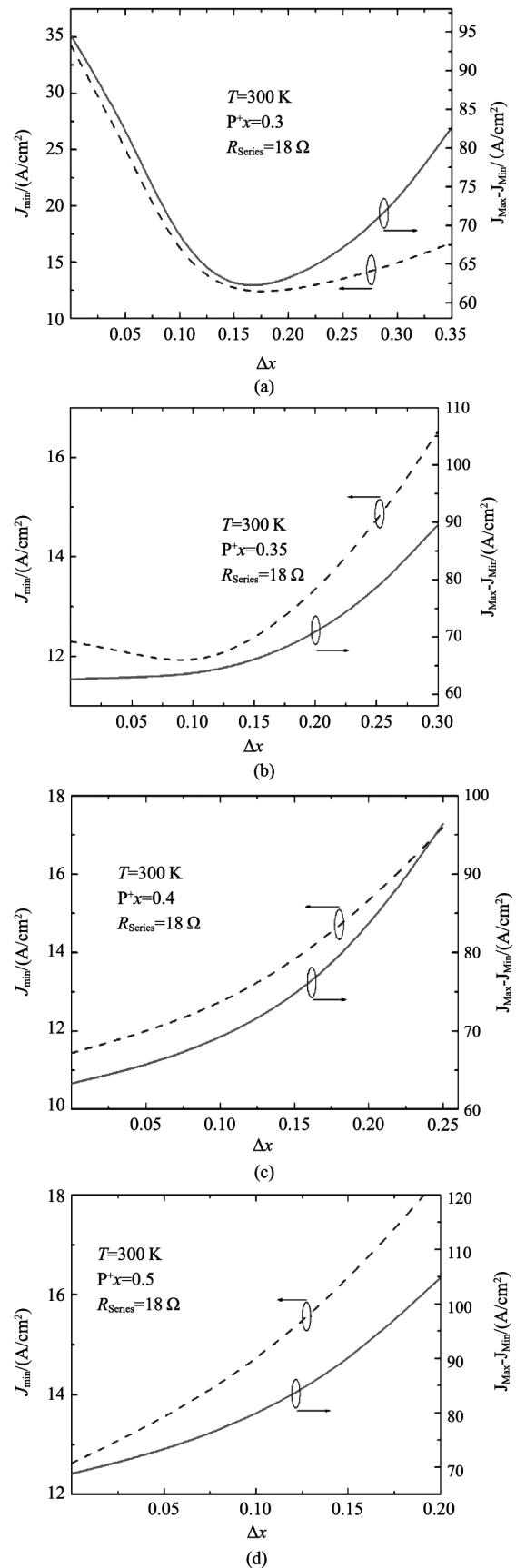quilibrium operation [J]. *J. Electron. Mater.*, 2008, **37**：
1362-1368.



Fig. 6    $J_{Min}$ and $J_{Max}$-$J_{Min}$ for P$^+$, $x = 0.3$ (a)；P$^+$, $x = 0.35$
(b)；P$^+$, $x = 0.4$ (c) and P$^+$, $x = 0.45$ for LWIR HgCdTe
heterostructure at $T = 300$ K and $R_{Series} = 18$ Ω

[6] Velicu S, Grein C H, Emelie P Y, *et al*. MWIR and LWIR HgCdTe infrared detectors operated with reduced cooling requirements [J]. *J. Electron. Mater.* , 2010, 39：873-881.

[7] Itsuno A M, Philips J D, Velicu S. Predicted performance improvement of Auger-suppressed HgCdTe photodiodes and p-n heterojunction detectors [J]. *IEEE Trans. Electron Dev.* , 2011, **58**：501-507.

[8] Kocer H. Numerical investigation of Auger contributed performance loss in long wavelength infrared HgCdTe photodiodes [J]. *Solid-State Electron.* , 2013, **87**：58-63.

[9] Norton P. HgCdTe infrared detectors [J]. *Opto-Electron. Rev.* , 2002, **10**：159-174.

[10] Rogalski A. HgCdTe infrared detector material：history, status and outlook [J]. *Rep. Prog. Phys.* , 2005, 68：2267-2336.

[11] Piotrowski A, Kłos K, Gawron W, *et al*. Uncooled or minimally cooled 10 μm photodetector with subnanosecond response time [J]. *Proc. SPIE*, 2007, 6542：65421B.

[12] Piotrowski A, Piotrowski J, Gawron W, *et al*. Extension of usable spectral range of Peltier cooled photodetectors [J]. *Acta Physica Polonica A*, 2009, **116**：52-55.

[13] Stanaszek D, Piotrowski J, Piotrowski A, *et al*. Mid and long infrared detection modules for picosecond range measurements [J]. *Proc. SPIE*, 2009, 7482：74820M.

[14] Piotrowski J, Gawron W, Orman Z, *et al*. Dark currents, responsivity and response time in graded gap HgCdTe structures [J]. *Proc. SPIE*, 2010, 7660：766031.

[15] Piotrowski A, Madejczyk P, Gawron W, *et al*. Progress in MOCVD growth of HgCdTe heterostructures for uncooled infrared photodetectors [J]. *Infrared Physics & Technol.* , 2007, **49**：173-182.

[16] Madejczyk P, Gawron W, Martyniuk P, Kębłowski A, Piotrowski A, Pusz W, Kowalewski A, Piotrowski J, Rogalski A. MOCVD grown HgCdTe device structure for ambient temperature LWIR detectors [J]. *Semicond. Sci. Technol.* , 2013, **28**(10)：105017.

[17] APSYS Macro/User's Manual ver. 2014, Crosslight Software, Inc, 2014.

[18] Casselman T N, Petersen P E. A comparison of the dominant Auger transitions in *p*-type (HgCd)Te [J]. *Solid State Commun.* , 1980, **33**：615-619.

[19] Hurkx G A, Klaassen D B M, Knuvers M P G. A new recombination model for device simulation including tunneling [J]. *IEEE Trans. Electron Devices*, 1992, **39**(2)：331.

[20] Hansen G L, Schmidt J L, Casselman T N. Energy gap versus alloy composition and temperature in $Hg_{1-x}Cd_xTe$ [J]. *J. Appl. Phys.* , 1982, **53**：7099.

[21] Scott W. Electron Mobility in $Hg_{1-x}Cd_xTe$ [J]. *J. Appl. Phys.* , 1972, **43**：1055-1062.

[22] Bhan R K, Dhar V. Carrier density approximation for non-parabolic and highly degenerate HgCdTe semiconductors [J]. *Semicond. Sci. Technol.* , 2004, **19**：413-416.

[23] Gupta S, Bhan R K, Dhar V. Unified carrier density approximation for non-parabolic and highly degenerate HgCdTe semiconductors covering SWIR, MWIR and LWIR bands [J]. *Infrared Phys. & Technol.* , 2008, **51**：259-262.

[24] Quan Z J, Chen G B, Sun L Z, *et al*. Effects of carrier degeneracy and conduction band non-parabolicity on the simulation of HgCdTe photovoltaic devices [J]. *Infrared Phys. & Technol.* , 2007, **50**：1-8.

[25] Wang J, Chen X, Hu W, *et al*. Temperature dependence characteristics of dark current for arsenic doped LWIR HgCdTe detectors [J]. *Infrared Phys. & Technol.* , 2013, **61**：157-161.

[26] Quan Z J, Chen X S, Hu W D, *et al*. Modeling of dark characteristics for long-wavelength HgCdTe photodiode [J]. *Opt Quant Electron*, 2007, **38**：1107-1113.

[27] Kocer H, Arslan Y, Besikci C. Numerical analysis of long wavelength infrared HgCdTe photodiodes [J]. *Infrared Phys. & Technol.* , 2012, **55**：49-55.